An Integrated 2D Ultrasound Phased Array Transmitter in CMOS with Pixel Pitch-Matched Beamforming

Costa, Tiago; Shi, Chen; Tien, Kevin; Elloian, Jeffrey; A. Cardoso, Filipe; Shepard, Kenneth

DOI
10.1109/TBCAS.2021.3096722

Publication date
2021

Document Version
Accepted author manuscript

Published in
IEEE Transactions on Biomedical Circuits and Systems

An Integrated 2D Ultrasound Phased Array Transmitter in CMOS with Pixel Pitch-Matched Beamforming

Tiago Costa, *Member, IEEE*, Chen Shi, Kevin Tien, Jeffrey Elloian, Filipe A. Cardoso and Kenneth L. Shepard, *Fellow, IEEE*

***Abstract*— Emerging non-imaging ultrasound applications, such as ultrasonic wireless power delivery to implantable devices and ultrasound neuromodulation, require wearable form factors, millisecond-range pulse durations and focal spot diameters approaching 100 µm with electronic control of its three-dimensional location. None of these are compatible with typical handheld linear array ultrasound imaging probes. In this work, we present a 4 mm x 5 mm 2D ultrasound phased array transmitter with integrated piezoelectric ultrasound transducers on complementary metal-oxide-semiconductor (CMOS) integrated circuits, featuring pixel-level pitch-matched transmit beamforming circuits which support arbitrary pulse duration. Our direct integration method enabled up to 10 MHz ultrasound arrays in a patch form-factor, leading to focal spot diameter of ~200 µm, while pixel pitch-matched beamforming allowed for precise three-dimensional positioning of the ultrasound focal spot. Our device has the potential to provide a high-spatial resolution and wearable interface to both powering of highly-miniaturized implantable devices and ultrasound neuromodulation.**

***Index Terms*—2D ultrasound phased-array, PZT integration, piezoelectric ultrasound transducers, phased-array beamforming, ultrasound neuromodulation, ultrasound powered implantable devices.**

I. Introduction

Leveraging decades of technological advances in the field of ultrasound medical diagnostic imaging, new ultrasound biomedical applications are now emerging, such as ultrasound neuromodulation [1-6] and ultrasonic power delivery and communication for medical implants [7-14]. These applications benefit from the attractive properties of ultrasound energy propagation and interaction with tissue, such as low scattering, low attenuation, and safe energy levels.

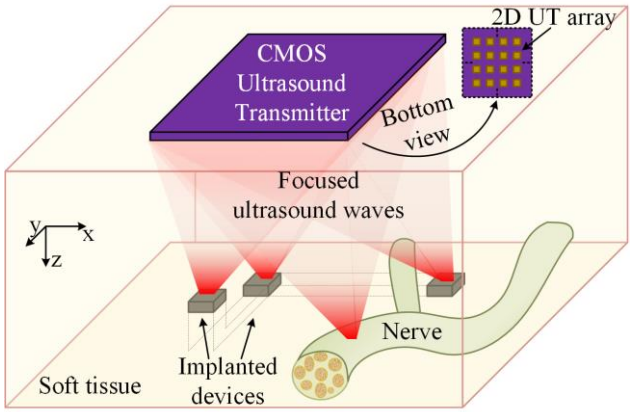

Fig. 1. Conceptual application of a wearable device performing ultrasound neuromodulation of a peripheral neve and powering implantable devices, with 3D control of focal sot location.

Furthermore, they require different ultrasound wave parameters when comparing to traditional ultrasound imaging applications. While in imaging short bursts of focused pulsed waves sequentially generated by subsections of a one-dimensional array can produce high-quality two-dimensional images, in both ultrasound neuromodulation and power delivery, long bursts of pulsed waves generated by all acoustic sources of a two-dimensional array with three-dimensional control of focal spot are required to achieve high spatial resolution and power efficiency [5, 11]. In addition, these applications would benefit significantly from wearable ultrasound phased-array form-factors, which are still far from the commercially available hand-held ultrasound phased-array probes. Such a form factor requires single-chip integration of the electronics for the device as well as the integration of transducer elements. This direct integration allows arrays to be sized to almost arbitrary scale and aspect ratios because of local interconnection between front-end electronics and transducer. It also allows ultrasound frequencies to be scaled higher towards smaller focal spots, both in supporting the tighter pitch required for transducer elements in this case and in reducing electrical parasitics

This work was supported by the DARPA ElectRX program (HR0011-15-2-0054).

T. Costa was the Bioelectronic Systems Lab, Department of Electrical Engineering, Columbia University, New York, NY 10027 USA. He is now with the Department of Microelectronics, Delft University of Technology, 2628 CD Delft, The Netherlands (e-mail: t.m.l.dacosta@tudelft.nl).

C. Shi, K. Tien, J. Elloian, F. A. Cardoso, and K. L. Shepard are with the Bioelectronic Systems Lab, Department of Electrical Engineering, Columbia University, New York, NY 10027 USA (e-mail: cs3184@columbia.edu; ktien@ee.columbia.edu; jelloian@ee.columbia.edu; fa2495@columbia.edu, shepard@ee.columbia.edu)

between the transducer and the front-end electronics which more significantly limit performance as the frequency is scaled. Smaller focal spots allow for more efficient powering of distributed sub-mm implantable devices, and also for higher-precision non-invasive neuromodulation of peripheral nerves. For neuromodulation applications in the brain, chip form-factors could also enable placement below the skull to allow for stimulating cortical circuits with high precision. This would alleviate the hurdles faced in transcranial ultrasound stimulation, where frequencies below 1 MHz are typically used to overcome the large acoustic attenuation in the skull, which reduces spatial resolution.

In the absence of commercially available phased-array technology matching the abovementioned requirements, researchers have been using commercially available single element focused transducers for these new non-imaging applications [1, 5, 11]. However, in addition to the very large size of these transducers, changing the focal spot location requires physically moving the transducer, necessitating the use of precise micro-manipulators, and, as a consequence, a more complex and bulky setup. These limitations of existing transducers are a major limiting factor in the advancement of emerging applications of ultrasound. The work presented here builds on prior efforts to develop miniaturized transducers with different form factors, such as disks [15], needles [16], flexible arrays [17-19] and IC 2D phased arrays [20-24]. However, unlike our proposed device, most of these systems do not allow electronic beam-steering for control of focal spot location [15, 16], still have large form factors [17] or are completely passive relying on extensive external electronics [18, 19]. IC 2D phased arrays, on the other hand, have been mostly designed for ultrasound imaging applications, by supporting only pulsed-wave operation [20-23] and having small transmitter apertures [21] in exchange for large receiving apertures towards high image quality. A 2D phased array with full transmitter aperture for brain stimulation has been recently proposed [24], however, ultrasound frequency is still limited to 2 MHz, which leads to focal spot dimensions in the millimeter range, still large in comparison with the scales of sub-mm ultrasound powered implantable devices and neuronal circuits.

In this article, we describe a 10 MHz 26 × 26 two-dimensional (2D) phased array ultrasound transmitter in a single-chip form-factor [25] in line with the "more-than-Moore" paradigm [26]. The transmitter is implemented as an integrated device with a 2D array of lead zirconate titanate (PZT) piezoelectric transducers directly microfabricated on top of a complementary metal-oxide-semiconductor (CMOS) integrated circuit (IC). PZT exhibits higher transmit electroacoustic sensitivity (S_{tx}) than capacitive and piezoelectric micromachined ultrasound transducers (CMUT, PMUT, respectively) [27, 28], which is critical for the applications targeted in this work. This direct integration leads to several orders of magnitude smaller form-factors when compared to commercially available transducers and a decrease of the parasitic capacitance for interconnection between transducer and transmitter circuits to only a few fF. This allowed the device to generate 10 MHz focused ultrasound waves with a pixel-level pitch-matched array of transmitter circuits occupying the full array aperture. These properties enable the individual configuration of the delay of each ultrasound transmitter with arbitrary pulse duration (*PD*), allowing for high-spatial-resolution volumetric control of the ultrasound focal spot in three dimensions.

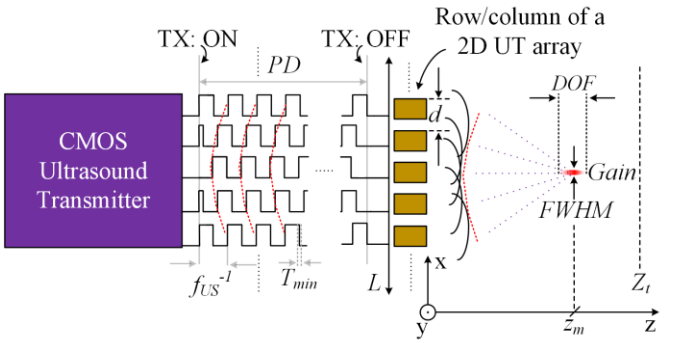

Fig. 2. 2D ultrasound phased array transmitter: properties of transducer driving signals, transducer array and focused ultrasound waves.

This article expands on our previous reporting on this design [25] by providing an in-depth system level analysis, a comprehensive PZT integration description and a detailed analysis of the experimental characterization. The organization of this article is as follows: Section II presents the system design of our approach. Section III analysis the choice of the ultrasound transducer material. Section IV discusses the circuit level design of the CMOS IC. Section V presents the experimental electrical characterization of the CMOS IC. Section VI introduces our method to integrate PZT transducers on top of CMOS ICs. Section VII presents the ultrasound characterization results, and Section VIII concludes the paper.

II. System Design

To be compatible with the requirements for ultrasound neuromodulation and ultrasound powered implantable devices (Fig. 1), the interfacing IC needs to allow for precise phase control of the driving signals of each transducer while allowing arbitrary *PD*. In contrast to ultrasound imaging applications, where pulsed waves must be generated, in this application, continuous-wave signals are desirable, both for allowing higher available power in ultrasound powered implantable devices [7, 9-11], and for meeting the *PD* specifications of ultrasound neuromodulation [1]. In such a continuous-wave mode, an arbitrary *PD* is easily achieved with a single enable input signal, rather than the more complex counter-based approaches required in pulsed-mode ultrasound [20]. In addition, these applications also demand a higher spatial resolution for the ultrasound focal spot, which can be achieved by increasing the ultrasound frequency. Here, continuous-wave beamforming can potentially lead to a design with a reduced area to accommodate the tighter pitch between the transducers, by exploring the periodicity of continuous ultrasound waves (Fig. 2). Finally, to maximize power delivery to implantable devices, and ensure successful neuromodulation, focal pressure should be maximized.

In Fig. 2, the relevant characteristics of focused ultrasound

waves, transducer geometry and driving signals are depicted. A CMOS ultrasound transmitter is programmed to generate driving signals with a given frequency (f_{US}), *PD*, and a delay with a given timing resolution (T_{min}). Each signal is applied to a piezoelectric transducer within a 2D array organization with an aperture L and an inter-element pitch d. With carefully defined delays for 2D beamforming [29], the piezoelectric transducers generate focused ultrasound waves at a pre-determined depth (Z_m, up to a maximum Z_t) and steering angle, in both the XZ (θ_{XZ}) and YZ planes (θ_{YZ}). The focal spot properties are characterized by the full width at half maximum (*FHWM*), the depth of field (*DOF*) and the focusing gain (*Gain*). The interplay between the abovementioned characteristics must be understood. The main design variables influencing the focal spot characteristics are the wavelength of the ultrasound waves (λ) and L. λ is readily derived from f_{US} and the speed of sound in soft tissue (~1540 m/s). L, on the other hand, is given by:

$$L = d \times \left(\sqrt{N} - 1\right) \tag{1}$$

Where N is the number of transducers of a squared 2D phased array. To avoid grating lobes in the field of view of the transducer array, d must respect the condition given by (2), where θ_{max} is the maximum of θ_{XZ} and θ_{YZ} [30]. For θ_{max} of ±90°, d has a minimum value at $\lambda/2$.

$$d = \frac{\lambda}{1 + \sin\left(\theta_{\max}\right)} \tag{2}$$

The focal spot properties *FHWM*, *DOF*, Z_t and *Gain* relate to λ and L as shown in (4), (5), (6), and (7), respectively.

$$FWHM \propto \frac{\lambda Z_m}{L} \tag{3}$$

$$DOF \propto \frac{\lambda {Z_m}^2}{L^2} \tag{4}$$

$$Z_t \approx \frac{L^2}{\pi\lambda} \tag{5}$$

$$Gain \propto \frac{L}{\lambda Z_m} \tag{6}$$

From (*3*)-(*6*), it can be concluded that it is advantageous to decrease λ and increase L, since it leads to lower *FHWM* and *DOF* and larger Z_t and *Gain*. However, the scattering and absorption of ultrasound waves in the propagation path leads to attenuation in the acoustic pressure, which increases linearly with distance and exponentially with frequency at a rate of approximately 0.75 dB/cm/MHz in soft tissue [31]. Also, from (2), decreasing λ results in a smaller d, leading to lower area budget for each transmitting circuit channel. In addition, increasing L also leads to larger number of N, as seen from (1), which, for a given power budget for the CMOS ultrasound transmitter, reduces the available power/channel. Selecting λ should take into account the abovementioned tradeoffs in relation to the target applications in this paper. Implantable

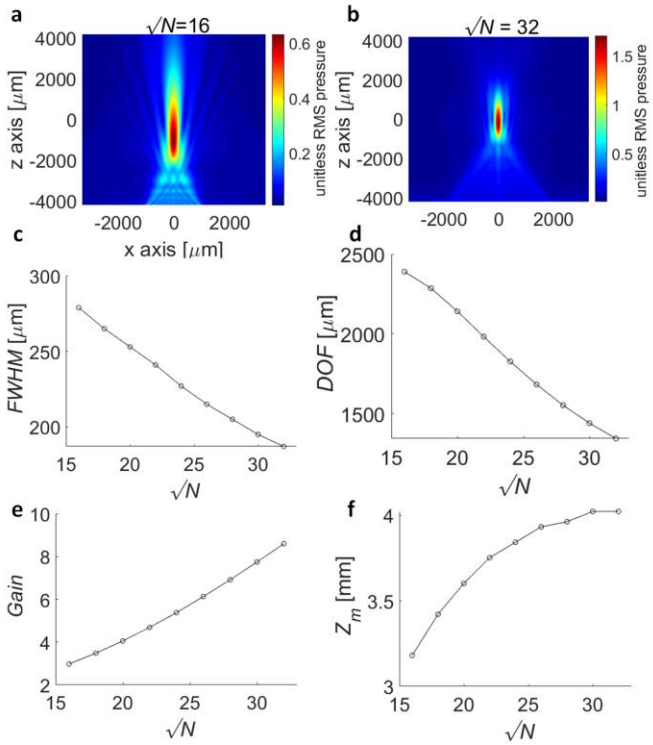

Fig. 3. Focusing properties of integrated 2D ultrasound phased arrays. a,b, simulated beam profiles of an ultrasound wave with N of 5 mm generated by a 16x16 2D ultrasound array (a) and 32x32 2D ultrasound array (b). c,d,e,f, influence of array aperture on *FWHM* (c), *DOF* (d), *Gain* (e) and Z_m (f).

devices featuring ultrasound power delivery and data telemetry have recently evolved into the sub-mm scale, with sizes as small as 380 µm × 300 µm × 570 µm [13]. On the other hand, in the micrometer scales of neuronal circuits both in the CNS and PNS demand matching spatial resolution from neuromodulation devices. For these reason, λ was set to 150 µm, which in soft tissue translates into an f_{US} of 10 MHz.

To properly dimension the optimal L, its influence on the focal spot dimensions properties was evaluated through k-wave [32] simulations. A squared 2D array of N ultrasound sources was interfaced with a medium modelled with the acoustic properties of soft tissue. Each source was configured to generate ultrasound waves with unitary pressure, and with a specific delay to produce a focal spot with Z_m of 5 mm, with both θ_{XZ} and θ_{YZ} of 0° [29]. The selected Z_m is in accordance with applications targeted in this paper for small animal studies. To eliminate grating lobes, d was set to 75 µm, which corresponds to λ/2 at 10 MHz (2). The effect of L on the focal spot properties was simulated by sweeping N from 16 x 16 to 32 x 32 (1), with the results showed in Fig. 3. *FWHM* and *FOD* correspond to the dimensions within 3dB of the maximum focal pressure. From Fig. 3a and Fig. 3b, the different properties of the focal spot for the minimum and maximum simulated values of N are evident, with increasing N leading to a lower *FWHM* (Fig. 3c), *DOF* (Fig. 3d) and higher *Gain* (Fig. 3e). One important observation from the simulations is the focal depth shift, which is common in arrays with small Fresnel numbers, leading to a discrepancy between the geometrical Z_m of 5 mm and the actual Z_m of approximately 4 mm [33]. To minimize this

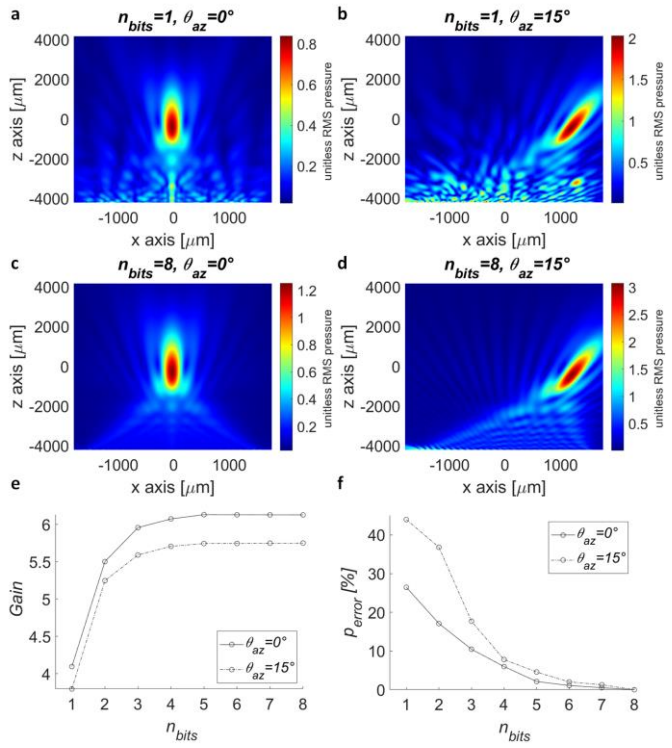

Fig. 4. Influence of timing resolution on the focal spot properties. a,b simulated beam profiles of an ultrasound wave with N of 5 mm generated by a 26x26 2D ultrasound array with 1 bit (a) and 8 bit (b) of timing resolution. c,d, influence of timing resolution in f_g (c) and in the normalized beam profile p_{ratio} (d).

error, N was set to 26 x 26. Increasing N further produced negligible improvements in the simulated Z_m while increasing the total number of transducers and circuit area, which, for a given total power budget, leads to a tighter power/channel ratio.

All of the abovementioned trade-offs assume that T_{min} is low enough to generate the precise phasing for focal spot generation. As lower T_{min} requires higher timing resolution in the transmitting circuit, and, consequently, higher circuit area, the effect of T_{min} on the focal spot properties must also be determined. The number of bits of precision (n_{bits}) was defined as:

$$n_{bits} = \log_2\left(\frac{1}{f_{US}T_{\min}}\right) \tag{7}$$

k-wave simulations were performed for a 26×26 array configured for a geometric Z_m of 5 mm, θ_{YZ} *of 0*° and θ_{XZ} of 0° and 15° and and n_{bits} spanning from 1 to 8 bits. The beam profile for the extreme cases (n_{bits} = 1 and n_{bits} = 8) are shown in Fig. 4a-d, where an increase of approximately 30% in the *Gain* is observed for 8 bits, with the trend shown in Fig. 4c. In addition, with n_{bits} equal to 1, unwanted acoustic wave constructive interferences appear in locations outside of the focal spot (Fig. 4a,b). These can lead to unwanted effects, such as powering up an incorrect device in a distributed implantable device scheme, or interact with unwanted neuronal circuits. These unwanted effects where quantified by the error of the maximum of the pressure difference between the beam profile for varying n_{bits} (p_{nbits}) and the beam profile for 8 bits (p_{8bits}), which corresponds to the focal spot pressure:

$$p_{error} = \frac{\max\left(p_{nbits} - p_{8bits}\right)}{\max\left(p_{8bits}\right)} \times 100 \tag{8}$$

Fig. 4f shows the variation of p_{error} for different n_{bits}, where it can be seen that for n_{bits} greater than 6, negligible improvements are obtained. Hence, n_{bits} was set to 6, since it maximizes *Gain* and minimizes acoustic wave constructive interferences at locations outside of the focal spot.

III. Ultrasound Transducer Material

The most common types of transducers used in ultrasound phased arrays are either piezoelectric, in the form of bulk transducers or piezoelectric micromachined ultrasound transducers (pMUTs), or capacitive micromachined ultrasound transducers (cMUTs). Piezoelectric transducers are still the most widely used transducer type. In the form of bulk transducers, they typically use the inverse piezoelectric effect of PZT ceramics, which convert an applied AC signal into thickness mode vibration, generating acoustic waves. PZT is characterized by high S_{tx}, high quality factor (Q), and a high acoustic mismatch with soft tissue, typically requiring an acoustic matching layer to increase the transmission efficiency and an acoustic backing layer if increased bandwidth is required, such as in the case of ultrasound imaging applications. In pMUTs, on the other hand, transduction is performed by application of an AC signal across a suspended piezoelectric flexural membrane, typically of PZT or aluminum nitride (AlN) [34]. Since pMUT membranes are softer than bulk PZT, they inherently increase the acoustic matching with soft tissue without requiring acoustic matching layers. However, the S_{tx} of pMUTs is still much lower than of bulk PZT transducers [28, 34], making pMUTs more appropriate in sensing applications [35]. Similarly to pMUTs, cMUTs also operate with suspended flexural membranes, and have the advantage of using membrane materials compatible with the CMOS manufacturing process, such as silicon nitride. Traditionally, cMUTs are characterized with a lower S_{tx} when compared to PZT [27]; however, they have a much lower Q and, as pMUTs, higher acoustic matching with soft tissue [36]. For ultrasound imaging applications, the lower Q of cMUTs leads to great advantage over piezoelectric transducers, since it allows for an inherently better axial resolution. On the other hand, for the applications targeted in this work, the high S_{tx} of PZT leads to the generation of higher acoustic intensities at the focal spot, while its higher Q enables higher power efficiency in the acoustic transmission [15].

Bulk PZT transducers are still preferable to cMUTS when high S_{tx} and Q are required. While it has been shown that cMUTs can be optimized to have a S_{tx} similar to that of bulk PZT [37] by using substrate-embedded springs, if PZT is acoustically matched with soft tissue, its effective S_{tx} increases beyond that of cMUTs [38]. Also, advanced ceramic-based piezoelectric materials such as Lead Magnesium Niobate/Lead Titanate (PMN-PT) provide an opportunity to boost the effective S_{tx} approximately 3 to 5 times compared with PZT [39].

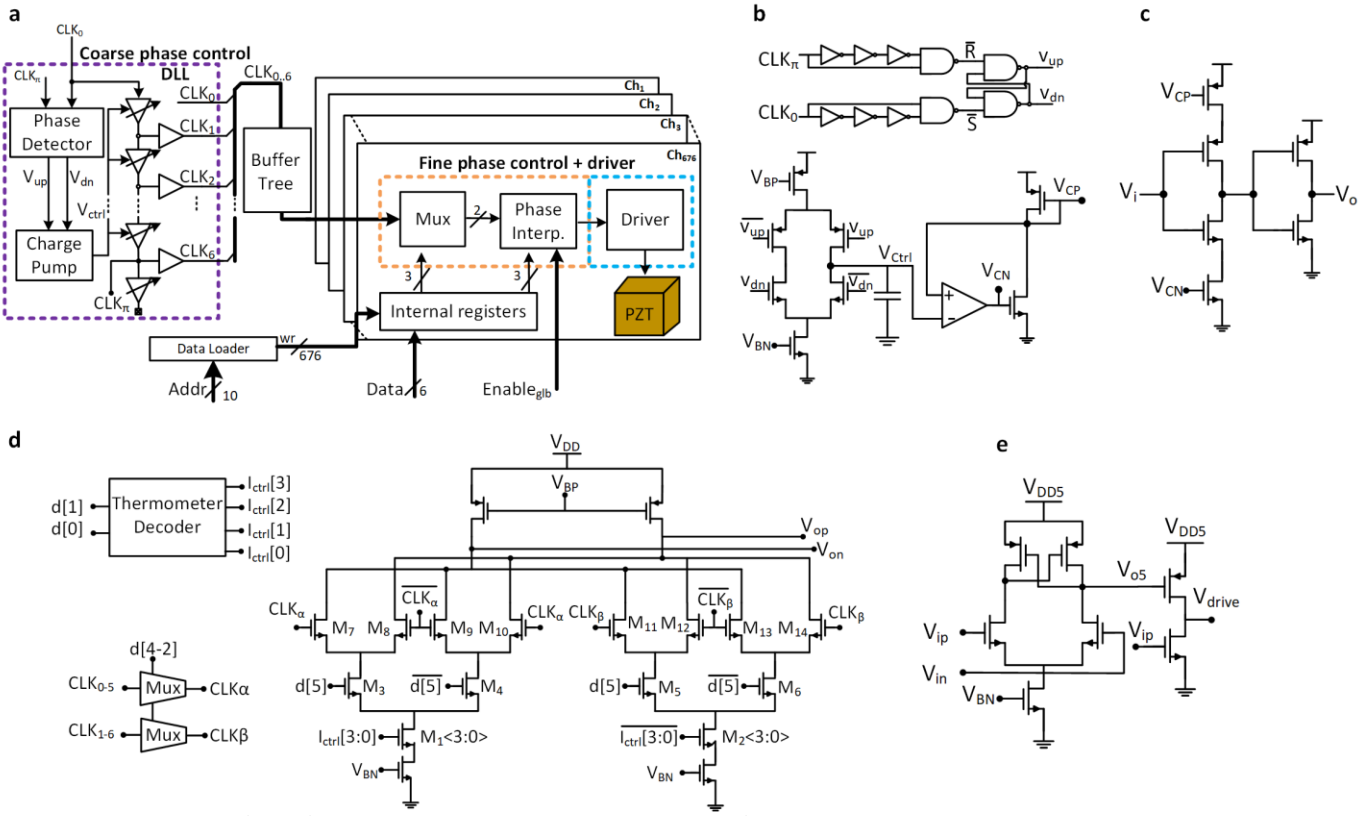

Fig. 5. IC with transmit beamformer for 2D ultrasound phased arrays. **a**, block diagram of IC showing the coarse phase control and the transmit channels composed by the fine phase control and driver. b,c, building blocks of the DLL: phase detector and charge pump(b), delay line element (c). d, transistor level schematic of phase interpolator used in the fine phase control section of each transmit channel. e, transistor level schematic of the transmit channel driver, composed by a level shifter and a class-D amplifier.

IV. IC Design

The IC electronics (Fig. 5a) transform an externally supplied input clock signal (CLK_0) into 26 × 26 driving signals, each one with the appropriate phase to implement a transmit beamformer [29]. The IC was designed in two separate sections, a central coarse phase control unit, and an array of 26 × 26 transmit channels, featuring a fine phase control unit and a driver [25]. This solution provides a balance between having a central beamforming unit, which would create a complex routing problem, and having the beamforming circuit in each channel, which would require more circuit area per channel and reduce the scalability of the operating frequency. To configure all the internal registers with all the beamforming phase information, a data loader digital block was also included.

The coarse phase control unit is implemented by a delay locked loop (DLL) with the architecture shown in Fig. 5a. By applying an input CLK_0, the DLL generates six output clocks with an incremental 30° phase difference to CLK_0 ($CLK_{1\text{-}6}$), from 30° up to 180°, which at 10 MHz represents a time resolution of 8.3 ns. The phase detector supplies the inputs to the charge pump (Fig. 5b). The charge pump biasing current is 6.4 µA, and with a load capacitance of 7.2 pF, the DLL locks the phase of CLK_0 and CLK_π (unbuffered version of CLK_6 as seen in Fig. 5a) in less than 1 µs, for a frequency of 10 MHz. The output of the charge pump (V_{ctrl}) is converted into biasing voltages V_{CP} and V_{CN} by using the replica biasing circuit, which bias the current-starved voltage-controlled inverter in the delay elements, as shown in Fig. 5c. Each current-starved inverter in series with a standard inverter in the six-element delay line consumes a dynamic current of 16 µA in the locked state at 10 MHz. To minimize the loading differences between the delay element outputs, a dummy delay element is added at the last stage of the delay line. CLK_0 and $CLK_{1\text{-}6}$ are fed into the transmit channel array and to minimize clock skew, a clock buffer tree is designed using a distributed buffer scheme.

The fine-phase control circuit (Fig. 5d) includes a register where the 6 bits corresponding to the phase are stored ($d_{5\text{-}0}$). Two input multiplexers select two clocks with consecutive phases (CLK_α and CLK_β) using $d_{4\text{-}2}$, and uses a phase interpolator to generate an output differential signal with a fine-tuned phase [40]. $d_{1\text{-}0}$ is thermometer-coded to control the tail current of differential pairs $M_{7\text{-}14}$. The tail current value is 43 µA, with an LSB of 10.75 µA, which corresponds to a phase resolution of 7.5° and T_{min} of 2.08 ns. Since the DLL outputs only cover the phases from 0° to 180°, the phase interpolator expands the phase map from 0° to 360°. This is done through transistors $M_{3\text{-}6}$, controlled by d_5 to steer the tail current between two sets of differential pairs, one set for an output phase in the quadrants from 0° to 180° ($M_{7,8}$ and $M_{11,12}$), and the other set for an output phase-shifted to the quadrants from 180° to 360° ($M_{9,10}$ and $M_{13,14}$).

All of the phase control circuitry operates at a 1.8-V power supply. A driver circuit in each transmit channel, consisting of

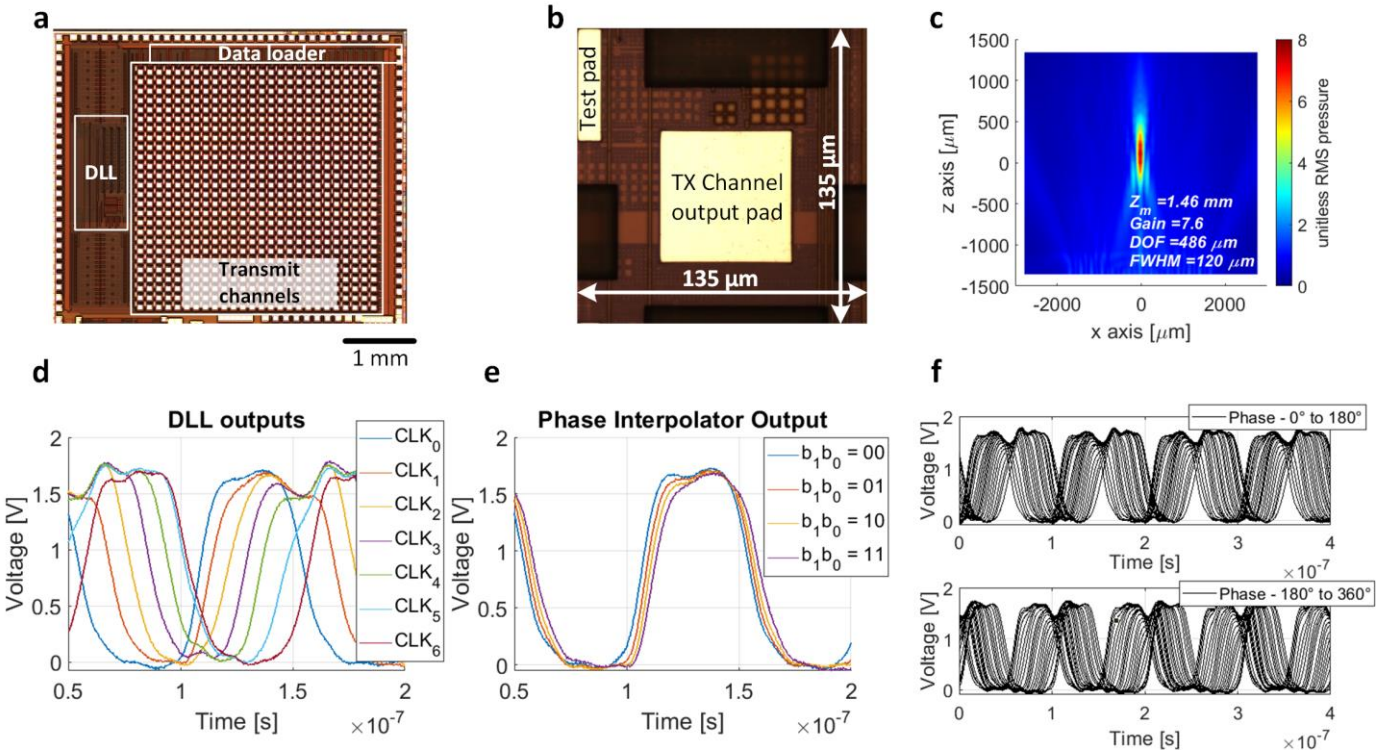

Fig. 6. Electrical experimental characterization of the IC. a, microphotograph of fabricated IC, with an area of 4 mm × 5 mm, and a transmit array area of 3.75 mm × 3.75 mm. b, microphotograph of a single transmit channel. c, simulated beam profile for a 26 × 26 ultrasound transducer array with a geometrical focal spot *N* of 2 mm, with ideal acoustic signals. d, DLL output signals with a 10-MHz CLK generated by the FPGA as the DLL input. e, output of the phase interpolator of ch_0 with the 4 possible output phases. CLK_α and CLK_β digital configured to be equal to the DLL outputs corresponding to CLK_0 and CLK_1. f, complete phase sweep for ch_0.

a level shifter and Class-D amplifier, boosts the voltage up to 5 V to drive the transducer (Fig. 5e).

V. Electrical Characterization

The IC, a microphotograph of which is shown in Fig. 6a as manufactured in a TSMC 180 nm 1.8/5V process, occupies an area of 5 mm × 4 mm. The transmit channel was designed in a 2D array with a *d* of 135 µm (Fig. 6b), hence, some degree of grating lobes were expected, however, k-wave simulations using a 26x26 array of acoustic sources with a *d* of 135 µm revealed that the peak pressure of grating lobes is negligible when compared with the pressure at the focal spot (Fig. 6c). The die was wirebonded to a custom PCB socket and encapsulated with a UV curable epoxy. The PCB socket connects to a test motherboard, which features a Spartan-6 FPGA development board (Opal Kelly XEM6310). The measurement results presented here were obtained by supplying the IC with a 10-MHz input CLK, divided in the FPGA from a 100 MHz low-jitter oscillator (0.5 ps_{RMS}), and by direct probing the output pads of each transmitter connected to the corresponding driver circuit. Given the jitter of the input CLK being 3 orders of magnitude lower than T_{min}, we have neglected its effect. For simplicity, the high voltage supply of the IC is shared with the core supply voltage of 1.8 V.

We first characterized the output timing characteristics of the coarse and fine phase control of the first channel in the array (ch_0), by sweeping the corresponding phase control bits. The outputs of the coarse phase control were recorded (Fig. 6d) at the ch_0 output with bits $d_{5,1,0}$ set to 0 to select the outputs of the DLL. The average time delay between the coarse phase control outputs was 8.76 ns with a standard deviation of 1.7 ns. It is of note that this measurement also takes into account the clock buffer network that connects the outputs of the coarse phase control to each transmission channel. The phase interpolator outputs of ch_0 (Fig. 6e) represent the phase interpolation between the first two outputs of the DLL, CLK_0 and CLK_1, selected with $d_{5\text{-}2}$ set to 0. The results shown in Fig. 6e reveal an average delay resolution of 1.6 ns with a standard deviation of 0.28 ns, which, again, includes any possible clock skew from the distributed clock buffer tree.

To analyze the transmitter channel performance across the array, 16 channels equally spaced across the array were measured by sweeping the input phase control bits. The results for the first measured channel are shown in Fig. 6f, split between 0° to 180° and 180° to 360°. The delay transfer

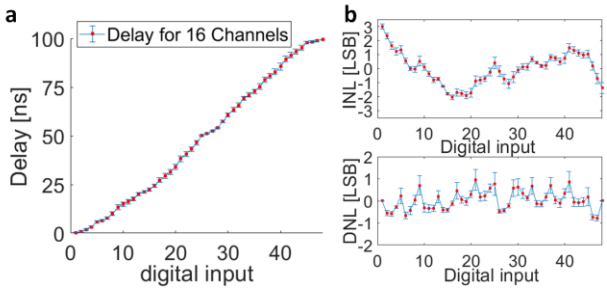

Fig. 7 delay transfer function for 16 channels equally spread across the array. a, average (red) and standard deviation (blue) values for the measured 16 channels. b, average (red) and standard deviation (blue) values of INL and DNL of the delay transfer function shown in (a)

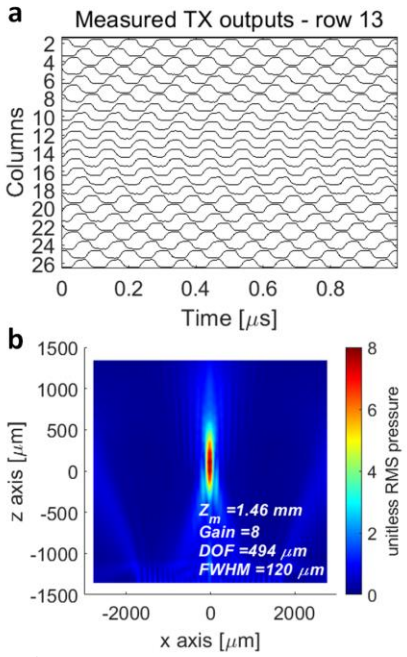

Fig. 8 Beam profile simulation using measured electrical signals as acoustic sources for a focal depth of 5 mm. a Signals of row 13. b, Beam profile

function for all the measured channels is displayed in Fig. 7a, revealing a monotonic characteristic. Further analysis of the data of Fig. 7a reveals an average resolution of 2.12 ns, which is close to the designed value of 2.08 ns, with a standard deviation of 0.94 ns. The integral nonlinearity (INL) and differential nonlinearity (DNL) of the transfer curve of Fig. 7a are shown in Fig. 7b. While the average DNL is less than 1 LSB, which guarantees monotonicity, there is a larger INL, of up to 3 LSBs.

To understand the impact of the INL of the designed system in its ability to perform beam steering and on the focal spot characteristics, the IC was programmed to generate driving signals corresponding to *N* of 2 mm with a steering angle of 0°, and all the outputs were measured for a duration of 1 µs, as illustrated in Fig. 8a for row 13. Similarly to the simulation done in Fig. 6c, a k-wave simulation was then performed for a 26 × 26 2D array of acoustic sources, with 135 µm pitch, 10 MHz operating frequency, using the signals measured from the IC as acoustic sources. The simulated beam profile is shown in Fig. 8b, including the calculated focal spot parameters. Comparing with the simulation with ideal sources of Fig. 6c, it can be seen that the non-linearity of the transmitter channel transfer function, and other nonidealities such as clock skew

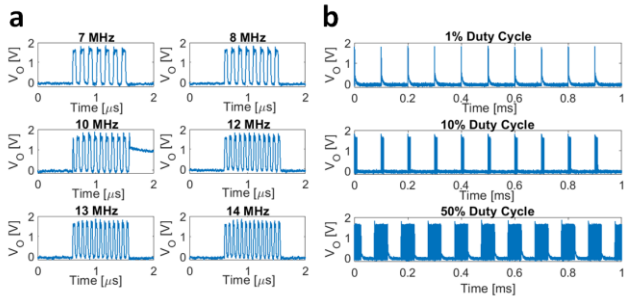

Fig. 9 Output of ch_0 for different input CLK frequencies (a) and duty cycles (*PD*) (b)

from the DLL outputs to transmitter array, had no effects on *FWHM* and Z_m, and negligible effects on *DOF* and *Gain*, with a difference between simulations with ideal and measured signals of only 1.6% and 5%, respectively.

The IC was also characterized for operating frequencies from 7 MHz to 14 MHz, with 1 µs PD measured at the output of ch_0, as shown in Fig. 9a. The ability of the IC to operate at frequencies around the central frequency of 10 MHz adds the flexibility of interfacing with ultrasound transducers with slightly different resonance frequencies. In the case of bulk piezoelectric transducers such as PZT, the resonance frequency is directly related to the material thickness, which is dependent on manufacturing tolerances. *PD* can be arbitrarily set by setting the ON time of an enable signal, which is connected to all transmit channels, as shown in the measurement of Fig. 9b. Here, ch_0 was measured with a pulse repetition frequency (*PRF*) of 10 kHz and duty cycles of 1%, 10% and 50%, which correspond to *PD* of 1 µs, 10 µs and 50 µs, respectively. By decreasing the *PRF*, *PD* values in the millisecond range can be obtained, however, requiring careful monitoring of heat dissipation.

VI. Ultrasound Transducer Integration

The IC described here requires direct integration of ultrasound transducers with a footprint matched to the output pads of the array of transmitters (Fig. 6b). For that reason, we have developed an integration method for a 2D array of PZT transducers directly on top of the IC [25, 41] and illustrated in Fig. 10. The fabrication method follows a subtractive process, starting with a commercially available 7.24 × 7.24 cm^2 sheet of pre-polled 267-µm-thick PZT5A (piezo.com). The measured charge sensitivity of the bulk PZT5A was 360 pC/N (d33 meter, Piezotest). Contacts (10 nm of Cr followed by 100 nm of Au) were patterned on both sides of the sheet by using lift-off photolithography and e-beam evaporation (Fig. 11a). The PZT5A sheet was then cut into small chips matching the transmit array dimensions of 3.75 mm × 3.75 mm using a dicing saw process. Afterward, a PZT5A chip is pre-diced from one side by about 20% of its thickness using the same dicing saw process with a blade thickness of 50 µm, resulting in kerfs with a width of approximately 55 µm. Following this step, the CMOS chip I/O pads are protected with a thin layer of photoresist. Afterwards, an anisotropic conductive film (ACF, TFA220-8, H&S High Tech) was tacked to the surface of the

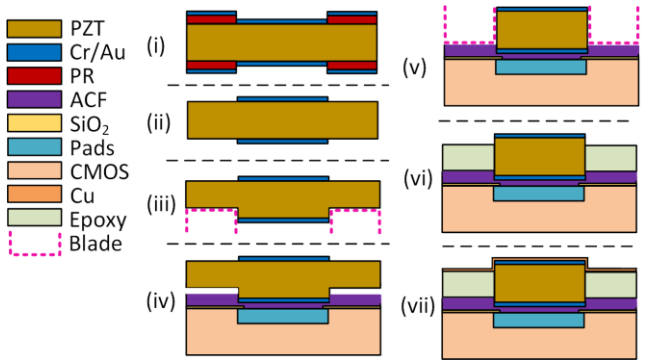

Fig. 10 Fabrication flow including PZT contact deposition (i) and patterning (ii), back side dicing (iii), adhesion to the CMOS chip using an anisotropic conductive film (ACF) (iv), PZT top side dicing (v), kerf filling (vi) and top metallization (vii)

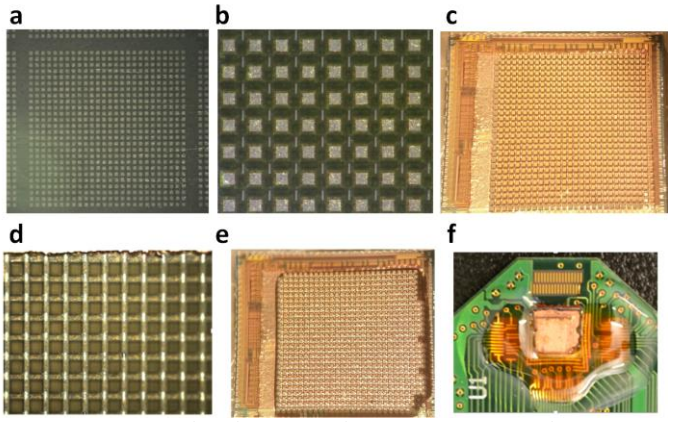

Fig. 11 Photographs of the fabrication of 2D PZT array on top of CMOS chip. a, PZT sheet with Cr/Au contacts. b, overlay of the CMOS and PZT released chip images for alignment. c, top view of the integrated chip after PZT top dice dicing. d, test pads on the CMOS chip revealing fully individualized PZT structures. e, chip after filling the PZT pillar kerfs with an epoxy through capillarity. f, top level metallization (Cu), wirebonding and encapsulation in a custom test PCB.

CMOS chip, centered with the array of transmitter output pads. By using a chip bonding tool (Fineplacer Lambda, Finetech), the CMOS and PZT5A chips are aligned with sub-µm precision (Fig. 11b), with the PZT5A pre-diced layer facing the CMOS chip surface. Given the conductive particle density of the ACF of 40000 pcs/mm^2, this leads to approximately 100 conductive particles for the CMOS pad dimensions of 50 x 50 µm^2. Hence, a lower precision alignment can be tolerated, as long as the higher contact resistance and lower current density does not lead to a decreased voltage across the PZT5A transducer; both chips are then bonded by thermo-compression, with a force of 150 N and 175 °C for 15 seconds. Both temperature and pressure were calibrated to ensure that a monolayer of conductive particles is created at the interface between the PZT5A and the CMOS chip pads.

The PZT5A chip was then diced from the top with the 50-µm-thick blade going through 90% of the original thickness, leading to individual PZT5A pillars without damaging the CMOS chip surface. The actual pillar kerfs were measured to be approximately 65 µm. The resulting fully diced transducers are shown in Fig. 11c, with Fig. 11d showing the CMOS chip surface, where the transmitter test pads are seen in the PZT5A array kerfs. From Fig. 11c, only two transducers are missing in the bottom right corner, which results in a yield of 99.7 %.

Finally, the pillar kerfs are filled with an epoxy to give mechanical stability to the array, and to serve as a supporting structure for the PZT5A transducer array top contact, as seen in Fig. 11e. The ground connection for the 2D pillar array is implemented by sputtering a 500-nm layer of copper on top of the chip, as seen in Fig. 11f. By using a probe station measurement system, it was confirmed that the ground plane was connected to all pillar structures. The final step consisted of lifting-off the photoresist covering the CMOS chip I/O pads, for subsequent wirebonding. The fully fabricated chip is also shown in Fig. 11f, with the chip wirebonded and encapsulated to a custom test PCB. Given that the piezoelectric effects of PZT5A can be degraded by exposure to high temperatures [42], all the fabrication steps involving temperatures above 100 °C were individually verified to have no effects on the piezoelectric properties of the PZT material.

VII. Ultrasound Experimental Characterization

To validate both the fabrication method and the interface between the IC and the 2D ultrasound transducer array, an ultrasound experimental test setup was implemented (Fig. 13a). The IC was encapsulated and interfaced as described in section VI, with the high voltage supply shared with the 1.8 V core supply, for simplicity. The PCB socket with the fabricated device was immersed into a 3D-printed container filled with distilled water and connected to the test motherboard. A hydrophone (HGL-0200 – OndaCorp), connected to an amplifier with 20 dB of gain (AG-2010 - OndaCorp), is attached to a three-axis motorized stage (MTS50/M-Z8 – Thorlabs) and immersed in the distilled water bath at the center of the array. The hydrophone has an aperture of 200 µm and an acceptance angle of 100°, with the amplifier ensuring a flat frequency response up to 40 MHz. The stage controller outputs a digital signal that is high when the stage is moving, which is connected to an oscilloscope (Keysight MSO-X 4054A) to provide synchronization between the hydrophone readout signal and its position. The IC transmitters are controlled by an enable signal (TX_{enable}), which is used as the trigger signal for the hydrophone readout. The stage controller, oscilloscope, and FPGA are connected to a computer by USB, where a graphical user interface is used to control all the components of the measurement. A photograph of part of the measurement setup is shown in Fig. 13b.

The resonance frequency of the transducer was obtained by measuring the frequency of maximum output pressure. This was done by sweeping the driving frequency of the transducers and measuring the output pressure of the array with the hydrophone, with the result shown in Fig. 13c. The maximum pressure was achieved for a 8.4 MHz, which was set as the working frequency for the next steps in the device characterization. The IC was then programmed to output a planar wave, with all transmitter channels generating the same driving signal and with a *PRF* of 10 kHz and a duty cycle of 1%, corresponding to *PD* of 1 µs. To decouple ultrasound waves from any capacitive coupling from the IC driving signals and the hydrophone tip electrode, the hydrophone was placed 2 mm away from the fabricated device, which corresponds to approximately 1.3 µs of the ultrasound propagation time (larger than *PD*). The motorized stage was programmed to scan an area of 5 mm x 5 mm in the XZ plane with steps of 100 µm, and the oscilloscope was programmed to record the peak to peak acoustic pressure for each step of the hydrophone. The resulting beam profile can be found in Fig. 14a, showing a uniform pressure level across the measured area below 10 kPa. The next step consisted of programming the IC to generate driving signals corresponding to a focal depth of 5 mm, θ_{YZ} of 0°, and θ_{XZ} of 0°, -15°, and 15°, following the same recording procedure as with the planar wave test. The resulting beam profiles are shown in Fig. 14b-d, clearly showing the generation of focused ultrasound waves. With a maximum focal pressure of approximately 40 kPa with a 1.8 V driving voltage for the 0° case, and slightly less for the -15° and 15° angles, as expected. Since pressure scales linearly with the driving voltage, the

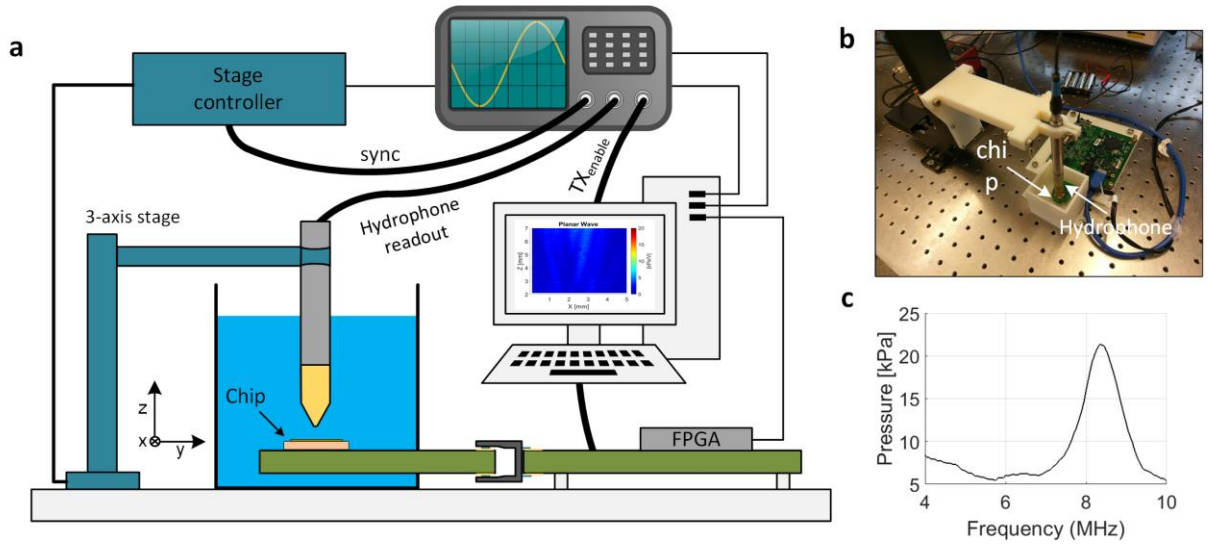

Fig. 13 Diagram of the ultrasound characterization setup (a), photograph of the test setup showing the motorized stage, hydrophone, container and chip (b). pressure variation with driving frequency (c).

maximum driving voltage of 5 V leads to a maximum focal pressure of approximately 100 kPa. Higher focal pressure in the MPa range can be achieved if higher transducer driving voltages are used, if PMN-PT piezoelectric materials are employed instead of PZT5A, or if acoustic matching layers are added. Higher driving voltage can be used with standard low voltage CMOS processes by using stacked driving schemes [43], opposing to the area-consuming high-voltage DMOS transistors found in BCD processes. This further supports the high-frequency nature of this work, which requires low-area beamforming and driving circuits.

The focal spot dimensions *FWHM* and *DOF* are 215 µm and 1.68 mm, respectively, which is larger than the values obtained from simulations for the same L, f_{US}, and Z_m, as seen in Fig. 3. This is also evident in Fig. 12, where the three measurements for focused waves are overlapped, showing only the measurements within -3-dB of the maximum pressure from each beam profile. Given the larger step size (100 µm) used in the hydrophone scan, a comparison cannot be made with the same precision; however, for a θ_{az} of 0°, *FWHM* is between 300 µm and 400 µm, and *DOF* is approximately 4 mm. For θ_{az} of -15° and 15°, the measured *FHWM* is between 100 µm and 200 µm, which is in line with simulations shown in Fig. 3; however, *DOF* cannot be measured since it expands to a region closer to the IC that cannot be accurately measured.

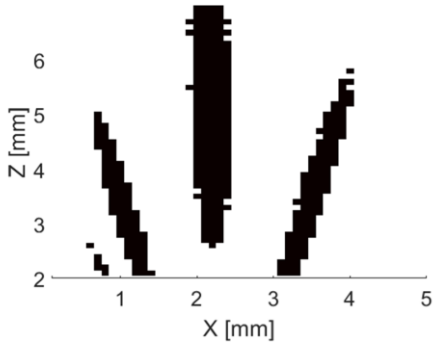

Fig. 12 Overlapped beam profiles of the focused ultrasound waves, emphasizing the -3dB focal spot area.

One possible source for this discrepancy is that not all of the elements in the transducer array are making electrical contact with the respective transmitter output pads, leading to a smaller active array area, which leads to larger values for *FWHM* and *DOF*. However, the measured Z_m of 4 mm is close to the simulated value of 3.93 mm. Since the focus shift due to the Fresnel number of the ultrasound array depends on the active array area, a smaller active area would lead to a lower measured Z_m, which is not observed. Given that the driving signals from the IC result in approximately equal simulated beam profiles when compared with the ideal case, as shown in Fig. 6c and Fig. 8b, the more likely cause of the difference in focal spot dimensions is mechanical effects from the silicon substrate or the epoxy filling the array kerfs, which were not modeled. Further studies are required to provide more understanding of these effects, to further decrease the focal spot dimensions closer to the simulated values.

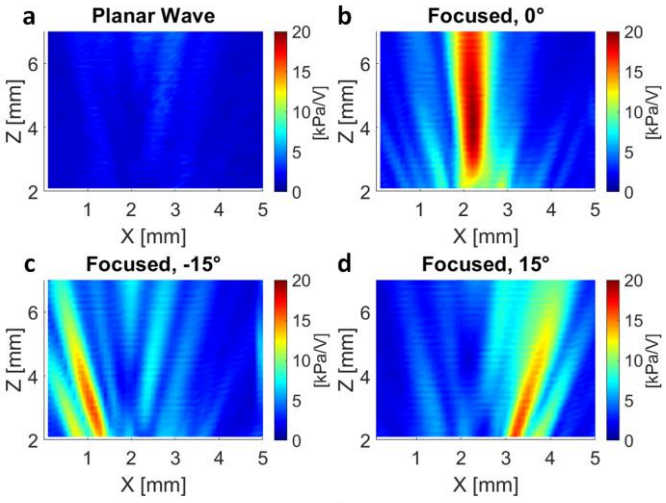

Fig. 14 Measured ultrasound beam profile in the ZX plane, with planar wave (a), and with geometrical focus depth of 5 mm and steering angle of 0° (b), -15° (c) and 15°(d).

TABLE I
COMPARISON OF THIS WORK WITH THE STATE OF THE ART

	[17]	[20]	[21]	[24]	This work
Application	Imaging and neuromodulation	Imaging	Imaging	Neuromodulation	Neuromodulation and wireless powering
CMOS Process	Discrete	0.25 µm HV	0.18 µm LV	0.18 µm HV	0.18 µm LV
Transducer	PZT	CMUT	PZT	CMUT	PZT
Integration	NA	Flip-chip	Flip-Chip	Flip-chip	Flip-chip
Chip area	NA	9.2x9.2 mm^2	6.1x6.1 mm^2	8x8 mm^2	5x4 mm^2
Power/channel	NA	4.5 mW	0.27 mW	NA	1.5 mW
Center freq.	1.3 MHz	5 MHz	5 MHz	2 MHz	8.4 MHz
# of Tx el.	8 – 1D	1024 – 2D	64-off chip	1024 – 2D	676 – 2D
Full apert. TX	Yes	Yes	No	Yes	Yes
Arbitrary PD	Yes	No	No	Yes	Yes
Focal pressure	1.6 MPa	N/A	300 kPa	574 kPa	40 kPa (up to 100 kPa)
Focal depth	3 cm	N/A	5 cm	0.5 cm	0.5 cm
Driving voltage	20 V	55 V	50 V	60 V	5 V
S_{tx}	80 kPa/V	N/A	6 kPa/V	9.5 kPa/V	Up to 20 kPa/V

VIII. CONCLUSIONS

We have presented an integrated 2D ultrasound phased-array transmitter in CMOS that enables the use of miniaturized ultrasound devices for emerging applications such as ultrasound neuromodulation and ultrasonic powering of implantable devices. The first key innovation resided on the in depth analysis of the system-level design, by relating the ultrasound focal spot properties, the 2D phased array geometry, and the required timing resolution for the transmit beamforming circuits. We often see ultrasound phased array systems with hundreds and even more than one thousand channels, without understanding the trade-offs of such systems. Our analysis methodology allowed us to exactly specify the required ultrasound transducer geometry, frequency, and timing specifications of the beamforming electronics. The second innovation consisted of a mixed-signal continuous-wave beamforming approach for the driving circuits, opposing to the more conventional digital approach [20, 24], which avoids the need of higher clock frequencies for the same timing resolution. In addition, it allowed for arbitrary pulse durations with a simple internal register controlled by a common enable signal. This lead to a circuit implementation of a 2D array with full-aperture pitch-matched transmitters towards a tighter pitch between transmit channels and transducers. The third key innovation was seen in our direct integration method of PZT on top of the CMOS IC. Since the transducer pitch is inversely proportional to the ultrasound frequency, the use of interposers or high-density conductive epoxies imposes a limitation in the minimum transducer pitch. Here, we used a thin and low-density ACF, consisting of 3 µm conducting particles allowing for down to sub-30 µm spacing. In our dicing process, since the ACF is too thin to protect the IC, we created a back-side/top-side dicing scheme, enabled by aligning top and back-side patterned features in the PZT. This allowed us to dice 2D ultrasound arrays of arbitrary number of elements with no risk of damage to the IC.

By exploring the capabilities of phased arrays, IC design, and direct integration of ultrasound transducers, we achieved the an integrated ultrasound transmitter device with 2D pixel pitch-matched transmit beamforming at the full aperture, arbitrary PD and ultrasound frequency of 8.4 MHz, scalable up to 10 MHz with negligible grating lobes. Comparing with other works (Table I), the combination of these feature is unique. An increased ultrasound frequency translates into smaller ultrasound focal spot volume, which is aligned with the ever-shrinking sizes of implantable devices and high-precision neuromodulation. Even though the focal spot pressure obtained in this work is lower than that presented in [17], adding an acoustic matching layer to the transducers presented in this work can substantially improve the focal spot pressure, which can be even further increased by using area-efficient HV drivers and more advanced piezoelectric materials such as PMN-PT. If higher driving voltages and long pulse durations are used, heat dissipation must be monitored to ensure that temperature remains within tolerable levels. Furthermore, the target applications also require structural ultrasound imaging, which was not the focus of this work. Since the imaging specifications would require lower-frame rates compared to traditional ultrasound imaging, we foresee that a sub-set of the transmitting channels could also include a receiver front-end to implement a synthetic aperture scheme.

Thinning of the CMOS substrate will allow this device to be rendered mechanically flexible [44]. In this way, we can envisage the emergence of wearable ultrasound patches for high-precision and non-invasive neuromodulation of peripheral nerves and for powering sub-mm implantable devices for both

therapeutic and diagnostic applications, which will be focus of future work.

ACKNOWLEDGMENT

We acknowledge the use of the Columbia Nano Initiative (CNI) cleanroom at Columbia University and the clean room of the Advanced Science Research Center (ASRC) at City University of New York.

[1] W. Legon *et al.*, "Transcranial focused ultrasound modulates the activity of primary somatosensory cortex in humans," *Nat Neurosci*, vol. 17, no. 2, pp. 322-9, Feb 2014

[2] J. Vion-Bailly, W. A. N'Djin, I. M. Suarez Castellanos, J.-L. Mestas, A. Carpentier, and J.-Y. Chapelon, "A causal study of the phenomenon of ultrasound neurostimulation applied to an in vivo invertebrate nervous model," *Scientific Reports*, vol. 9, no. 1, p. 13738, 2019/09/24 2019

[3] W. J. Tyler, "The mechanobiology of brain function," *Nature Reviews Neuroscience*, vol. 13, no. 12, pp. 867-878, 2012/12/01 2012

[4] D. Folloni *et al.*, "Manipulation of Subcortical and Deep Cortical Activity in the Primate Brain Using Transcranial Focused Ultrasound Stimulation," *Neuron*, vol. 101, no. 6, pp. 1109-1116.e5, 2019/03/20/ 2019

[5] M. E. Downs, S. A. Lee, G. Yang, S. Kim, Q. Wang, and E. E. Konofagou, "Non-invasive peripheral nerve stimulation via focused ultrasound *in vivo* " *Physics in Medicine and Biology*, vol. 63, no. 3, p. 035011, 2018

[6] Y. Liu *et al.*, "Bidirectional Bioelectronic Interfaces: System Design and Circuit Implications," *IEEE Solid-State Circuits Magazine*, vol. 12, no. 2, pp. 30-46, 2020

[7] D. Seo, J. M. Carmena, J. M. Rabaey, E. Alon, and M. M. Maharbiz, "Neural Dust: An Ultrasonic, Low Power Solution for Chronic Brain-Machine Interfaces," *arXiv.org*, vol. q-bio.NC, no. April, 2013

[8] D. Seo *et al.*, "Wireless Recording in the Peripheral Nervous System with Ultrasonic Neural Dust," *Neuron*, vol. 91, no. 3, pp. 529--539, 2016

[9] B. C. Johnson *et al.*, "StimDust: A 6.5mm^3, wireless ultrasonic peripheral nerve stimulator with 82% peak chip efficiency," in *IEEE Custom Integrated Circuits Conference (CICC)*, 2018, pp. 1--4.

[10] Y. Zhang and K. L. Shepard, "A 0.6-mm2 Powering and Data Telemetry System Compatible with Ultrasound B-Mode Imaging for Freely Moving Biomedical Sensor Systems," in *2019 IEEE Custom Integrated Circuits Conference (CICC)*, 14-17 April 2019 2019, pp. 1-4, doi: 10.1109/CICC.2019.8780205.

[11] J. Charthad *et al.*, "A mm-Sized Wireless Implantable Device for Electrical Stimulation of Peripheral Nerves," *IEEE Transactions on Biomedical Circuits and Systems*, vol. 12, no. 2, pp. 257--270, 2018

[12] J. Vo, T. C. Chang, K. I. Shea, M. Myers, A. Arbabian, and S. Vasudevan, "Assessment of miniaturized ultrasound-powered implants: an in vivo study," *Journal of Neural Engineering*, vol. 17, no. 1, p. 016072, 2020

[13] C. Shi, T. Costa, J. Elloian, Y. Zhang, and K. L. Shepard, "A 0.065-mm(3) Monolithically-Integrated Ultrasonic Wireless Sensing Mote for Real-Time Physiological Temperature Monitoring," *IEEE Trans Biomed Circuits Syst*, vol. 14, no. 3, pp. 412-424, Jun 2020

[14] C. Shi *et al.*, "Application of a sub–0.1-mm3 implantable mote for in vivo real-time wireless temperature sensing," *Science Advances*, vol. 7, no. 19, p. eabf6312, 2021

[15] H. S. Gougheri, A. Dangi, S. Kothapalli, and M. Kiani, "A Comprehensive Study of Ultrasound Transducer Characteristics in Microscopic Ultrasound Neuromodulation," *IEEE Transactions on Biomedical Circuits and Systems*, pp. 1-1, 2019

[16] T. Choi, S. Bae, M. Suh, and J. Park, "A Soft Housing Needle Ultrasonic Transducer for Focal Stimulation to Small Animal Brain," *Annals of Biomedical Engineering*, 2019/12/13 2019

[17] V. Pashaei, P. Dehghanzadeh, G. Enwia, M. Bayat, S. J. A. Majerus, and S. Mandal, "Flexible Body-Conformal Ultrasound Patches for Image-Guided Neuromodulation," *IEEE Transactions on Biomedical Circuits and Systems*, pp. 1-1, 2019

[18] J. Lee *et al.*, "A MEMS ultrasound stimulation system for modulation of neural circuits with high spatial resolution in vitro," *Microsystems & Nanoengineering*, vol. 5, no. 1, p. 28, 2019/07/15 2019

[19] C. Wang *et al.*, "Monitoring of the central blood pressure waveform via a conformal ultrasonic device," *Nature Biomedical Engineering*, vol. 2, no. 9, pp. 687-695, 2018/09/01 2018

[20] A. Bhuyan *et al.*, "Integrated Circuits for Volumetric Ultrasound Imaging With 2-D CMUT Arrays," *IEEE Transactions on Biomedical Circuits and Systems*, vol. 7, no. 6, pp. 796--804, 2013

[21] C. Chen *et al.*, "A Front-End ASIC With Receive Sub-array Beamforming Integrated With a 32 x 32 PZT Matrix Transducer for 3-D Transesophageal Echocardiography," *IEEE Journal of Solid-State Circuits*, pp. 1--13, 2017

[22] D. Wildes *et al.*, "4-D ICE: A 2-D Array Transducer With Integrated ASIC in a 10-Fr Catheter for Real-Time 3-D Intracardiac Echocardiography," *IEEE Transactions on Ultrasonics, Ferroelectrics, and Frequency Control*, vol. 63, no. 12, pp. 2159-2173, 2016

[23] R. Wodnicki *et al.*, "Co-Integrated PIN-PMN-PT 2-D Array and Transceiver Electronics by Direct Assembly Using a 3-D Printed Interposer Grid Frame," *IEEE Transactions on Ultrasonics, Ferroelectrics, and Frequency Control*, vol. 67, no. 2, pp. 387-401, 2020

[24] C. Seok, O. Adelegan, A. O. Biliroglu, F. Y. Yamaner, and O. Oralkan, "A 2D Ultrasonic Transmit Phased Array Based on a 32x32 CMUT Array Flip-Chip Bonded to an ASIC for Neural Stimulation," in *IEEE International Ultrasonics Symposium (IUS)*, 2020 2020: IEEE.

[25] T. Costa, C. Shi, K. Tien, and K. L. Shepard, "A CMOS 2D Transmit Beamformer With Integrated PZT Ultrasound Transducers For Neuromodulation," in *2019 IEEE Custom Integrated Circuits Conference (CICC)*, 14-17 April 2019 2019, pp. 1-4, doi: 10.1109/CICC.2019.8780236.

[26] W. Arden, M. Brillouet, P. Cogez, M. Graef, B. Huizing, and R. Mahnkopf, "*More-than-Moore*, White Paper," [Online].Available: http://www.itrs2.net/uploads/4/9/7/7/49775221/irc-itrs-mtm-v2_3.pdf, 2019.

[27] I. Wygant, "A comparison of CMUTs and piezoelectric transducer elements for 2D medical imaging based on conventional simulation models," in *IEEE International Ultrasonics Symposium*, 2011.

[28] E. Ledesma *et al.*, "Squared PMUT with Enhanced Pressure Sensitivities," *Proceedings*, vol. 2, no. 13, p. 925, 2018

[29] L. Azar, Y. Shi, and S. C. Wooh, "Beam focusing behavior of linear phased arrays," *NDT and E International*, vol. 33, no. 3, pp. 189--198, 2000

[30] S.-C. Wooh and Y. Shi, "Optimization of Ultrasonic Phased Arrays," in *Rev. Prog. Quant. Nondestructive Eval.* : Springer, Boston, MA., 1998, pp. 883-890.

[31] M. C. Ziskin, "Fundamental physics of ultrasound and its propagation in tissue," *RadioGraphics*, vol. 13, no. 3, pp. 705-709, 1993

[32] *k-Wave*. (2009).

[33] K. Lou, S. Granick, and F. Amblard, "How to better focus waves by considering symmetry and information loss," *Proceedings of the National Academy of Sciences*, vol. 115, no. 26, p. 6554, 2018

[34] Y. Qiu *et al.*, "Piezoelectric Micromachined Ultrasound Transducer (PMUT) Arrays for Integrated Sensing, Actuation and Imaging," *Sensors*, vol. 15, no. 4, 2015

[35] X. Jiang *et al.*, "Monolithic ultrasound fingerprint sensor," *Microsystems & Nanoengineering*, vol. 3, no. 1, p. 17059, 2017/11/20 2017

[36] A. S. Ergun, G. G. Yaralioglu, and B. T. Khuri-Yakub, "Capacitive Micromachined Ultrasonic Transducers: Theory and Technology," *Journal of Aerospace Engineering*, vol. 16, no. 2, pp. 76-84, 2003

[37] C. B. Lee, A. Nikoozadeh, K. K. Park, and T. B. Khuri-Yakub, "High-Efficiency Output Pressure Performance Using Capacitive Micromachined Ultrasonic Transducers with Substrate-Embedded Springs," *Sensors*, vol. 18, no. 8, 2018

[38] Y. Wang *et al.*, "Magnesium Alloy Matching Layer for High-Performance Transducer Applications," (in eng), *Sensors (Basel, Switzerland)*, vol. 18, no. 12, p. 4424, 2018

[39] Z. Zhang *et al.*, "Design and comparison of PMN-PT single crystals and PZT ceramics based medical phased array ultrasonic transducer," *Sensors and Actuators A: Physical*, vol. 283, pp. 273-281, 2018/11/01/ 2018

[40] S. Sidiropoulos and M. a. Horowitz, "A semidigital dual delay-locked loop," *IEEE Journal of Solid-State Circuits*, vol. 32, no. 11, pp. 1683--1692, 1997

[41] C. Shi, T. Costa, J. Elloian, and K. L. Shepard, "Monolithic Integration of Micron-scale Piezoelectric Materials with CMOS for Biomedical Applications," in *2018 IEEE International Electron Devices Meeting (IEDM)*, 1-5 Dec. 2018 2018, pp. 4.5.1-4.5.4, doi: 10.1109/IEDM.2018.8614632.

[42] H. Jaffe and D. A. Berlincourt, "Piezoelectric transducer materials," *Proceedings of the IEEE*, vol. 53, no. 10, pp. 1372-1386, 1965

[43] A. Banuaji and H.-k. Cha, "A 15-V Bidirectional Ultrasound Interface Analog Front-End IC for Medical Imaging Using Standard CMOS Technology," *IEEE Transactions on Circuits and Systems II: Express Briefs*, vol. 61, no. 8, pp. 604--608, 2014

[44] S. Moazeni *et al.*, "19.2 A Mechanically Flexible Implantable Neural Interface for Computational Imaging and Optogenetic Stimulation over 5.4×5.4 mm 2 FoV," 2021: IEEE.